



Effect of Sintering Parameters on the Corrosion Characteristics of Iron-Alumina Metal Matrix Nanocomposites

Pallav Gupta¹, Devendra Kumar^{1*}, M.A. Quraishi², Om Parkash¹

¹Department of Ceramic Engineering, Indian Institute of Technology
(Banaras Hindu University), Varanasi-221005 (U.P.) - INDIA.

²Department of Chemistry, Indian Institute of Technology
(Banaras Hindu University), Varanasi-221005 (U.P.) - INDIA.

*Corresponding Author E-mail: devendra.cer@iitbhu.ac.in; Tel: (+91-542-6701792)

Abstract

The present paper reports the effect of sintering parameters (i.e. temperature and time) on the corrosion characteristics of Iron (Fe) – Alumina (Al₂O₃) metal matrix nanocomposites (MMNCs) synthesized by powder metallurgy (P/M) technique tested in freely aerated 1 N HCl solution and compared with that of pure iron specimen. The composite for the present investigation contains 10% Al₂O₃ and 90% Fe. The composites were prepared by ball milling followed by compaction and then sintering the specimens in an inert atmosphere in the temperature range of 900-1100°C for 1 to 3 hour. Phase and microstructure of the prepared nanocomposite specimens showed the presence of nano size iron aluminate (FeAl₂O₄) phase which is formed due to reactive sintering. It was found that the formation of nano iron aluminate improved the corrosion resistance of Fe-Al₂O₃ nanocomposites. XRD pattern of the corroded specimen showed the presence of aluminum chlorate (AlCl₃O₁₂) phase along with iron (Fe), aluminum oxide (Al₂O₃) and trace amount of iron chloride (FeCl₂) phases. SEM studies also showed the formation of nano size particles of constituent phases.

Keywords: Metal Matrix Nanocomposites (MMNCs); Powder Metallurgy (P/M); Tafel Polarization; X-ray diffraction (XRD) and Scanning Electron Microscopy (SEM).

1. Introduction

With technological progress in the present world, monolithic materials become insufficient to meet the increasing demands on product capabilities and functions. This incapability has led to the invention of some advanced materials which can serve with better structural, mechanical and electrochemical properties [1]. Metal Matrix Nanocomposites (MMNCs) is one such class of advanced material which possesses significantly improved properties including higher specific strength; specific modulus; damping capacity; good wear and corrosion resistance compared to unreinforced alloys [2]. There are several routes for the fabrication of the quality MMNC products. These include stir casting, powder metallurgy (P/M), chemical vapor deposition (CVD), physical vapor deposition (PVD) etc. [3-4]. Among these powder metallurgy (P/M) technique is used to develop quality MMNC products with more near net shaped object with utmost dimensional accuracy [5-7]. Another factor which plays an important role in the development of MMNCs is particle size and particle size distribution of the matrix and the reinforcement phases respectively [8-9]. There are a large number of reinforcements which are being embedded for formation of the MMNC products. A few of these include SiC, ZrO₂, WC etc [10]. Lot of work has been reported on the corrosion behavior of aluminium, magnesium and copper as the matrix material. However, no systematic attempt has been made to study the corrosion behavior of Al₂O₃ reinforced Fe metal matrix nanocomposites [11]. Candan et al. [12] reported the corrosion behavior of pure Al and Al-4 wt. % Mg alloy matrix composites comprising of 60 vol. % SiC particles. Composites were synthesized by pressure infiltration technique at 750°C. The corrosion tests were carried out in 3.5 wt. % NaCl environment up to 28 days. The weight loss of the composites increased with increasing time up to 3-5 days and then it remained constant. Scanning electron microscopy (SEM) analysis showed that Al-4 wt. % Mg alloyed matrix composite exhibited higher corrosion

resistance than pure Al matrix composite on the other hand potentiodynamic polarisation measurements showed higher i_{corr} values of Al-4 wt. % Mg alloyed matrix composites than pure Al matrix composites. Experimental results revealed that precipitation of Mg_2Si as a result of reaction between Al-Mg alloy and SiC particles has a beneficial effect on corrosion resistance of Al-4Mg alloy matrix composites due to interruption of the continuity of the matrix channels within the pressure infiltrated composites.

Effect of SiC phase on the corrosion behavior of SiC/Al metal matrix composites has been studied in 0.1 and 0.6N NaCl by Trzaskoma et al. [13] both in the presence and absence of dissolved oxygen. Anodic polarization behavior has been studied, and pitting potentials have been measured for three composite systems: SiC/Al 2024, SiC/Al 6061, and SiC/Al 5456. Corrosion behavior and the effects of anodizing on the corrosion resistance of the composites have been studied by a-c impedance techniques. The results show that pitting susceptibility is about the same for the composites and their corresponding alloys, except for Al2024. In this system, the composite is less resistant to pit initiation than the corresponding wrought aluminum alloy. Corrosion is more affected by the presence of oxygen than the SiC phase. In the absence of oxygen, corrosion resistance is improved for both the alloys and composites. It was also concluded that the corrosion resistance of the composites can be improved by anodizing.

Recently, an exhaustive amount of work on Fe- Al_2O_3 , Fe- ZrO_2 and CoO doped Fe- Al_2O_3 metal matrix composites have been done in our research group [14-18]. Various properties investigated include XRD, SEM, density, hardness, wear, compressive strength and corrosion. It was found from these studies that in Fe- Al_2O_3 and Fe- ZrO_2 metal matrix composites, due to reactive sintering process, a nano iron aluminate (FeAl_2O_4) and iron zirconium oxide ($\text{Zr}_6\text{Fe}_3\text{O}$) phase forms. This led to improvement in various properties. The reaction rate for the iron aluminate phase formation was reduced in CoO doped Fe- Al_2O_3 composites due to non reactive sintering but still the electrochemical properties were found to improve.

The present paper reports the effect of sintering parameters such as sintering temperature and time on the corrosion characteristics of Fe- Al_2O_3 metal matrix nanocomposites processed via Powder Metallurgy (P/M) Technique. The specimen was prepared by sintering in an argon atmosphere in the temperature range 900 - 1100°C for 1 to 3 hour respectively. The synthesized composite specimens showed the presence of nano size particles of iron aluminate phase which is formed due to reactive sintering between iron and alumina particles. Various corrosion characteristics investigated include corrosion potential (E_{corr}), corrosion current density (I_{corr}), corrosion rate (C_r) and corrosion protection efficiency (μ_p). It was found from the studies that the corrosion characteristics of the nanocomposites were much better than that of pure iron specimen. The improvement in the corrosion characteristics can be attributed to the presence of nano size iron aluminate phase. The present contribution also aims to investigate the electrochemical behavior of Fe- Al_2O_3 composite with increased addition of Al_2O_3 (10 wt%).

2. Experimental

Iron - alumina based MMNC specimens having composition of 90 wt % Fe (electrolytic grade with 99.5% purity) and 10 wt % Al_2O_3 (active; particle size of 70-230 mesh) were prepared using powder metallurgy technique. Green specimens prepared by compacting under a load of 7 tons were sintered in an argon atmosphere in the temperature range 900 - 1100°C for 1 - 3 hours. A nomenclature e.g. 10AFe1100(2) of different specimens is given indicating sintering temperature and time.

Studies on corrosion behavior of the specimens were performed using Gamry electrochemical cell having three electrodes connected to Gamry Instrument Potentiostat / Galvanostat with a Gamry framework system based on ESA400. Composite specimens were polished with emery polishing paper 600 no. and then with 12 μm diamond paste on a double disc polishing machine to remove any sort of stray marks from the surface of the specimen and to make it mirror polished. Gamry applications include software DC 105 for corrosion. Iron specimens with an exposed area of 1 cm^2 were used as working electrodes, platinum electrode was used as an auxiliary electrode, and standard calomel electrode (SCE) was used as reference electrode. All potentials were measured relative to SCE. Tafel curves were obtained by changing the electrode potential automatically from -250 to + 250 mV versus corrosion potential (E_{corr}) at a scan rate of 1mV s^{-1} .

Phase analysis of surface of corroded specimens was carried out by recording X-ray diffraction (XRD) patterns using Rigaku Desktop Miniflex II X-Ray diffractometer employing Cu-K α radiation with Ni-filter. **Microstructure** of the corroded surface of samples was studied using Inspect S-50, FP 2017/12 scanning electron microscope.

3. Results and Discussions

3.1 Tafel Polarization and Corrosion Behavior

The Tafel polarization curves of 10% Al₂O₃ reinforced specimens sintered for 3 different temperatures and time intervals are shown in Fig. 1, 2 and 3 respectively. Electrochemical parameters such as corrosion potential (E_{corr}), corrosion current density (I_{corr}), corrosion rate (C_p) and corrosion protection efficiency (μ_p) obtained from Tafel polarization curves are given in Table 1. Values of corrosion potential (E_{corr}), corrosion current density (I_{corr}), were evaluated from anodic and cathodic regions of Tafel plots. The linear segments of anodic and cathodic curves were extrapolated to obtain corrosion potential and corrosion current densities (I_{corr}). Protective efficiency was calculated from the measured I_{corr} values using the following relationship:

$$\mu_p \% = (I_{corr}^o - I_{corr}^i) / I_{corr}^o * 100$$

where I_{corr}^o and I_{corr}ⁱ are values of corrosion current density for pure iron and for specimens with aluminium oxide as reinforcement respectively.

Fig. 1 shows the tafel polarization plots of specimens 10AFe900(2), 10AFe1000(2) and 10AFe1100(2) sintered for 2h at different sintering temperatures. It is seen from these graph that corrosion potential (E_{corr}) for specimens 10AFe900(2), 10AFe1000(2) and 10AFe1100(2) is -577 mV, -540 mV and -531 mV respectively. It is also observed from Fig. 1 and table 1 that the corrosion rates of these three specimens are 803.2 mpy, 1542 mpy and 1955 mpy and the corrosion protection efficiency (μ_p) is found to be 99.12%, 98.32% and 97.87% respectively. Therefore, it can be concluded from the above discussion that the lowest corrosion rate as well as the highest corrosion protection efficiency was found for the specimen 10AFe900(2). It can be due to formation of an optimum amount of nano iron aluminate phase for this temperature and time of sintering. This formation by reaction between iron and alumina particles at sintering temperature of 900°C and for 2 hours of sintering time has lead towards the improvement in corrosion resistance of the nanocomposite specimen.

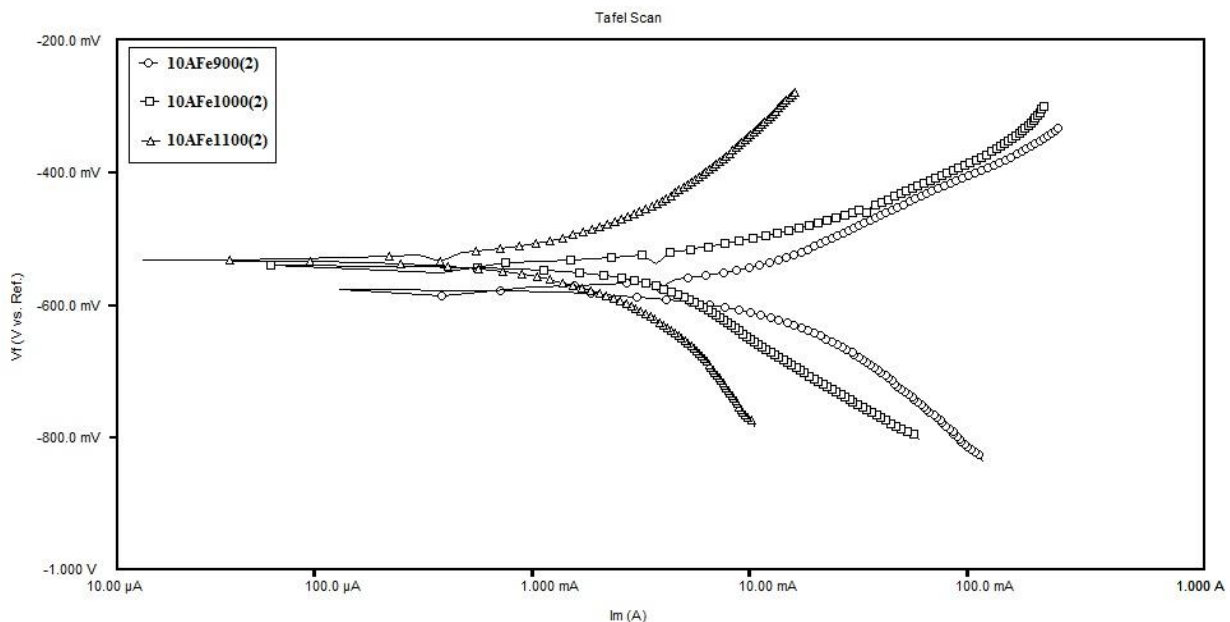


Figure 1: Tafel polarization plots of specimens 10AFe900(2), 10AFe1000(2) and 10AFe1100(2) sintered for 2h at different sintering temperatures.

Similarly, Fig. 2 shows the Tafel polarization plots of specimens 10AFe1000(1), 10AFe1000(2) and 10AFe1000(3) sintered at 1000°C for different sintering times. For these specimens the corrosion potential (E_{corr}) is found to be -611, -540 and -595 respectively [Figure 2 and Table 1]. The corrosion rate for all the three specimens namely 10AFe1000(1), 10AFe1000(2) and 10AFe1000(3) are found out to be 6049 mpy, 1542 mpy and 2491 mpy respectively. Further for these specimens the corrosion protection efficiency (μ_p) is found to be 93.43%, 98.32%

and 97.29% respectively. It can be concluded on the basis of the above results that for the sintering temperature of 1000°C and sintering time of 2 hours, the corrosion characteristics improve due to the formation of the same nano iron aluminate phase which forms due to reactive sintering but at the same time the corrosion protection efficiency for specimen 10AFe1000(2) is reduced by 0.8024% in comparison to the specimen 10AFe900(2).

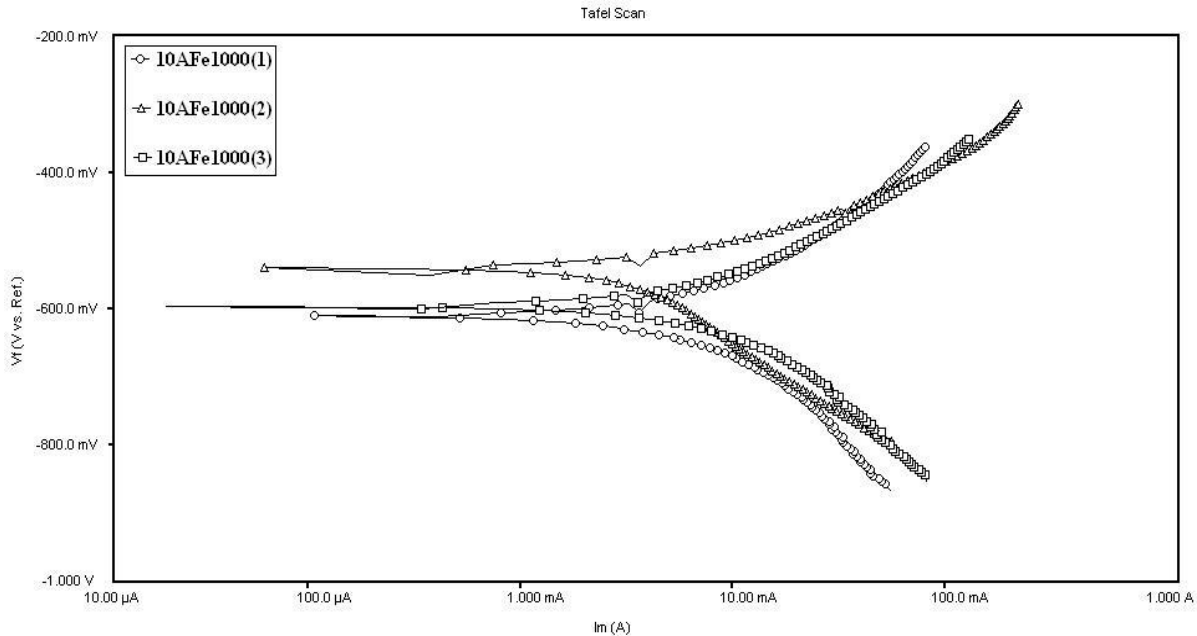


Figure 2: Tafel polarization plots of specimens 10AFe1000(1), 10AFe1000(2) and 10AFe1000(3) sintered at 1000°C for different sintering times.

Table 1: Electrochemical corrosion parameters and protective efficiency (μ_p) values for the various specimens in 1 N HCl solution.

Sl. No.	Sample Code	E_{corr} (mV)	I_{corr} (μ A)	Corrosion rate (C_r) (mpy)	μ_p (%)
1.	10AFe900(1)	-586	33900	30750	66.6
2.	10AFe900(2)	-577	1750	803.2	99.1
3.	10AFe900(3)	-581	55500	25480	72.3
4.	10AFe1000(1)	-611	6640	6049	93.4
5.	10AFe1000(2)	-540	1830	1542	98.3
6.	10AFe1000(3)	-595	3130	2491	97.3
7.	10AFe1100(1)	-606	36700	29380	68.1
8.	10AFe1100(2)	-531	2510	1955	97.9
9.	10AFe1100(3)	-586	5390	3878	95.8
10.	Pure Iron	-559	200000	92080	-

Fig. 3 illustrates the Tafel polarization plots of specimens 10AFe1100(1), 10AFe1100(2) and 10AFe1100(3) sintered at 1100°C for different sintering times. From Fig. 3 and table 1, these three specimens showed the corrosion potential (E_{corr}) values of -606 mpy, -531 mpy and -586 mpy respectively. The corrosion rate and corrosion protection efficiency (μ_p) of these three specimens namely 10AFe1100(1), 10AFe1100(2) and 10AFe1100(3) is found to be 29380 mpy, 1955 mpy and 3878 mpy and 68.09%, 97.87% and 95.78% respectively. From the above discussion it can be concluded that for 1100°C sintering temperature the best corrosion resistance is found for the specimen 10AFe1100(2).

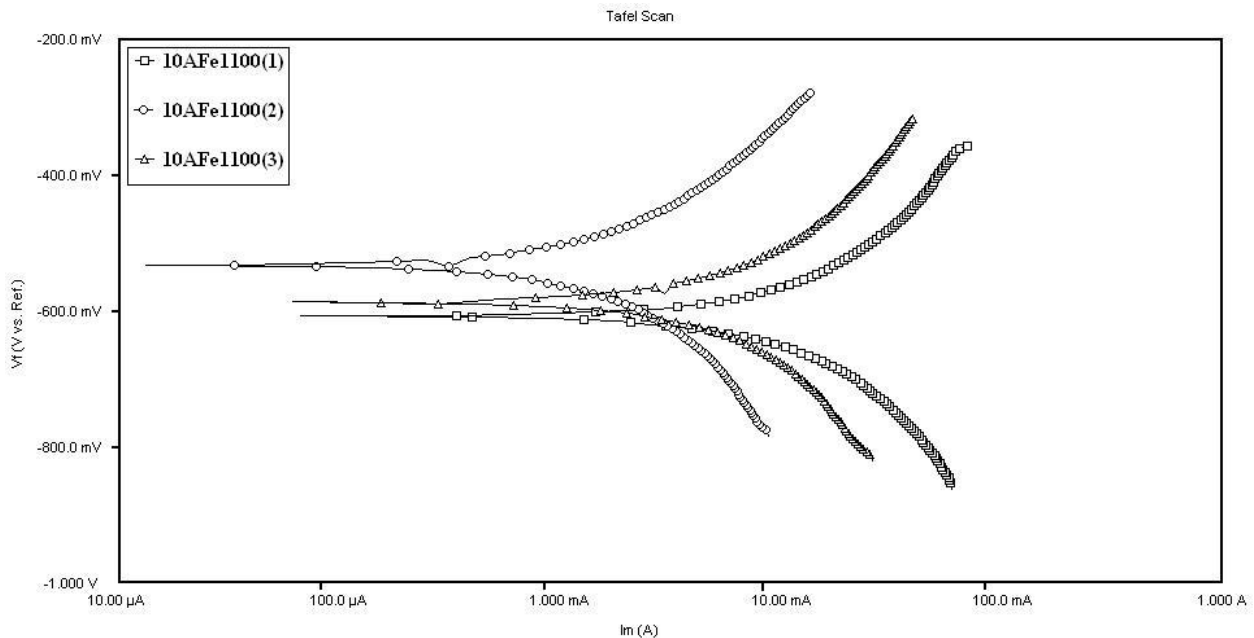


Figure 3: Tafel polarization plots of specimens 10AFe1100(1), 10AFe1100(2) and 10AFe1100(3) sintered at 1100°C for different sintering times.

Thus, on an overall basis it can be concluded that among the nine specimens synthesized at different sintering temperature and time the best corrosion characteristics are found for the specimen 10AFe900(2). The reason behind this can be that at lower sintering temperature of 900°C and sintering time of 2 hour, the reaction between iron and alumina particles is taking place due to which an optimum amount of nano size iron aluminate phase formation is taking place and this nano size phase is inhibiting the corrosion of the nanocomposite specimens.

It can also be seen from the tafel plots (Fig. 1, 2 and 3) and table 1 that in the presence of aluminium oxide (Al_2O_3) ceramic reinforcement, the tafel curves are shifted towards the lower current regions, showing the protective tendency of the nanocomposites. From the table 1 and figs. 1, 2 and 3 we observe that there is no definite trend observed in the E_{corr} values for the nanocomposite specimens. It suggests that addition of alumina particles in iron matrix and thereby formation of iron aluminate phase inhibits the corrosion of metal matrix nanocomposites. On the other hand it is very much interesting to note that the corrosion rate of the pure iron specimen was found to be 92080 mpy which is very much higher in comparison to the corrosion rate of the synthesized Fe- Al_2O_3 nanocomposite specimens. The best nanocomposite exhibited corrosion rate and corrosion protection efficiency value as 803.2 mpy and 99.12% respectively. On the basis of above discussion it can be concluded that due to the existence of anodic and cathodic areas on the iron surface it suffers corrosion. Pure iron forms ferrous ions and two electrons at anode and at cathode it combines with proton and forms hydrogen gas. But when iron is mixed with aluminium oxide, it leads to the formation nano iron aluminate phase on the surface of iron. The formation of nano size iron aluminate causes following changes:

- 1) Decreases Wettability.
- 2) Increases Hydrophobicity.
- 3) Reduces Roughness of the surface.

All the above three factors significantly reduce corrosion of the formed nanocomposite specimens. In all the synthesized specimen of 5% Al_2O_3 reinforced specimen the corrosion protection efficiency was found out to be above 90%. For 10% Al_2O_3 reinforced specimen the corrosion protection efficiency was found out to be above 90% for all the specimens except for the specimen 10AFe900(1) and 10AFe900(3).

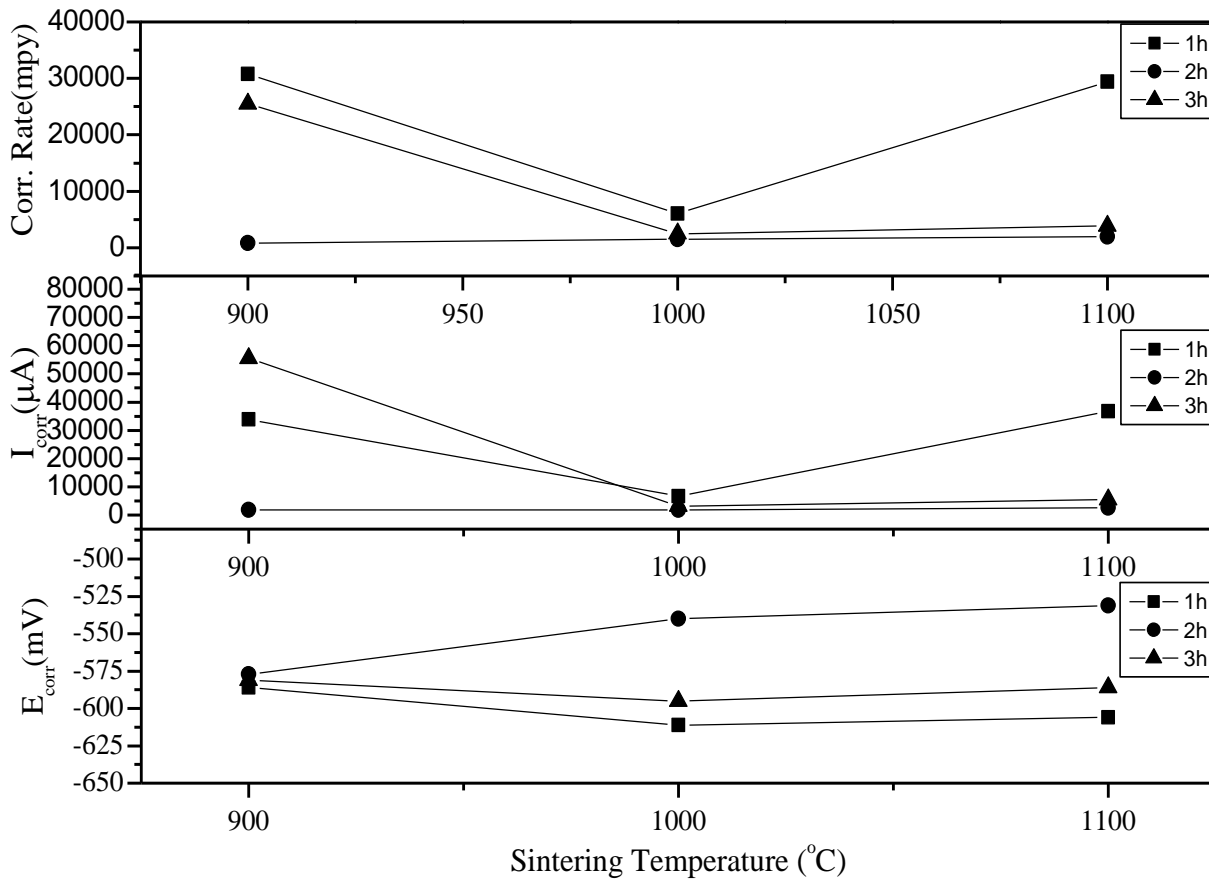


Figure 4: E_{corr} , I_{corr} and Corrosion Rate vs. Sintering Temperature plot for different sintering time intervals.

Fig. 4 shows the E_{corr} , I_{corr} and Corrosion Rate vs. Sintering Temperature plot for different sintering time intervals. Density and Hardness value of the specimen has been reported in our previous publication [19]. The density and hardness number of the specimens were found to be dependent on sintering and formation of iron aluminate ($FeAl_2O_4$) phase. This iron aluminate phase formation in turn depends upon sintering temperature and time respectively. It was found in the present study that the dependence of corrosion parameters such as I_{corr} and corrosion rate on sintering temperature and time is similar to that of the hardness number. At 1000°C sintering temperature the hardness number of the specimens sintered for 1h, 2h and 3h were found to be close to each other. The I_{corr} and corrosion rate of the specimen sintered at 1000°C for different time of sintering showed almost the same values. Therefore, it can be concluded that at 1000°C either we sinter the specimen for 1h, 2h or 3h the mechanical and electrochemical properties were found to improve due to an optimum formation of the iron aluminate phase.

3.2 Phase and Microstructure

Fig. 5 shows the XRD plots of specimen 10AFe900(1) and 10AFe900(2) after corrosion in 1N HCl solution respectively. Specimen 10AFe900(1) shows the presence of aluminium chlorate ($AlCl_3O_{12}$), iron chloride ($FeCl_2$), iron (Fe) and aluminium oxide (Al_2O_3) phases. It was also found that in this specimen the amount of the aluminium

chlorate was much more higher followed by some trace amount of iron chloride phase. Similarly XRD pattern of the specimen 10AFe900(2) also shows the presence of aluminium chlorate ($\text{AlCl}_3\text{O}_{12}$), iron chloride (FeCl_2), iron (Fe) and aluminium oxide (Al_2O_3) phases. On an overall basis it is found that the intensity of the aluminium chlorate is more in specimen 10AFe900(1) in comparison to the specimen 10AFe900(2).

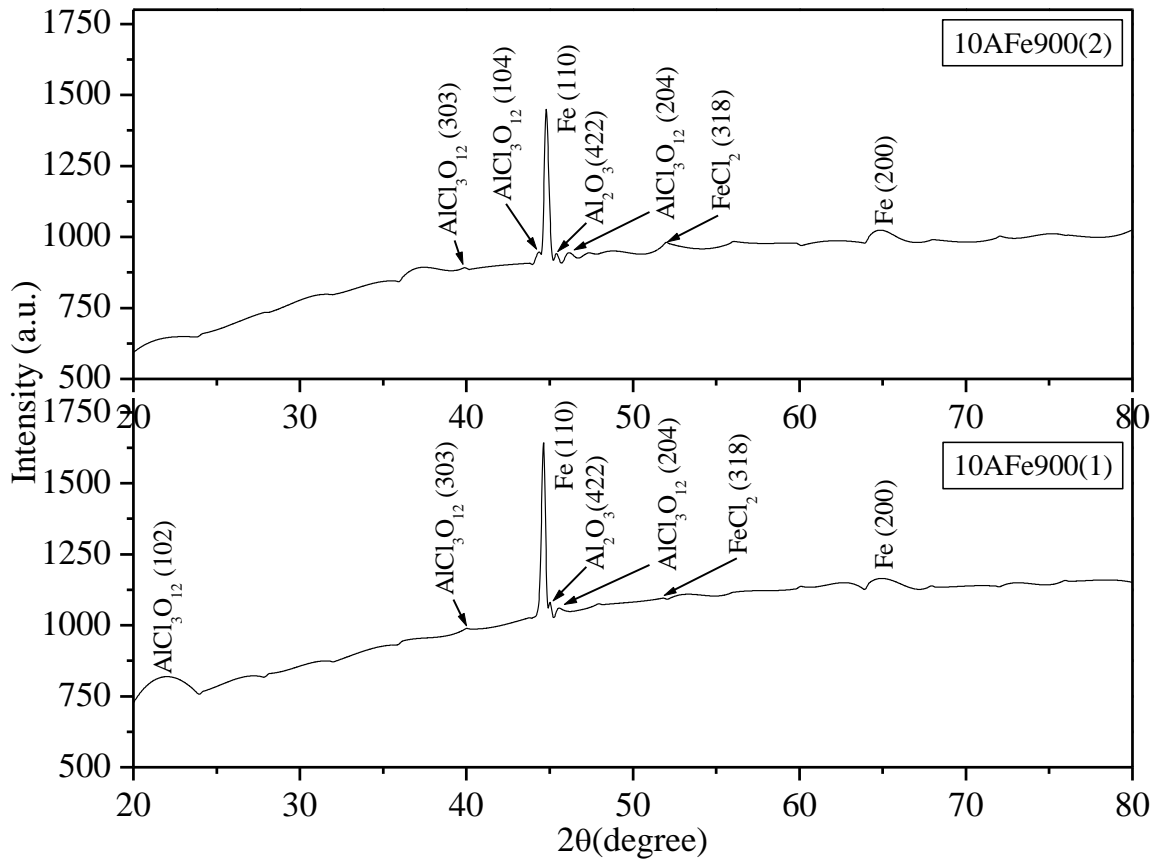


Figure 5: XRD plots of specimen 10AFe900(1) and 10AFe900(2) after corrosion in 1N HCl solution.

The amount of iron chloride phase is less in both the specimens. It is also seen that the corrosion rate of the specimen 10AFe900(1) is much more than that of the specimen 10AFe900(2) and thus due to this high corrosion rate, the formation of the aluminium chlorate phase is more in specimen 10AFe900(1) in comparison to the specimen 10AFe900(2). The chemical reaction between 1N HCl solution and alumina particles has led to formation of the aluminum chlorate phase respectively.

Fig. 6 shows XRD plots of specimen 10AFe1000(1) and 10AFe1100(2) after corrosion in 1N HCl solution. Both these specimens show the presence of the same phases which were present in the previous specimens i.e. aluminium chlorate ($\text{AlCl}_3\text{O}_{12}$), iron chloride (FeCl_2), iron (Fe) and aluminium oxide (Al_2O_3) respectively. It is seen from the plot that in the specimen 10AFe1000(1) after corrosion intensity of lines of aluminium chlorate phase is high while intensity for iron chloride is very small. Specimen 10AFe1100(2) also shows the presence of these two phases but the intensity of these phases is much lower than that of the specimen 10AFe1000(1). The specimen 10AFe1000(1) has higher corrosion rate in comparison to the specimen 10AFe1100(2). This seems that the amount of aluminium chlorate and iron chloride phases is more in specimen 10AFe1000(1) in comparison to specimen 10AFe1100(2) respectively.

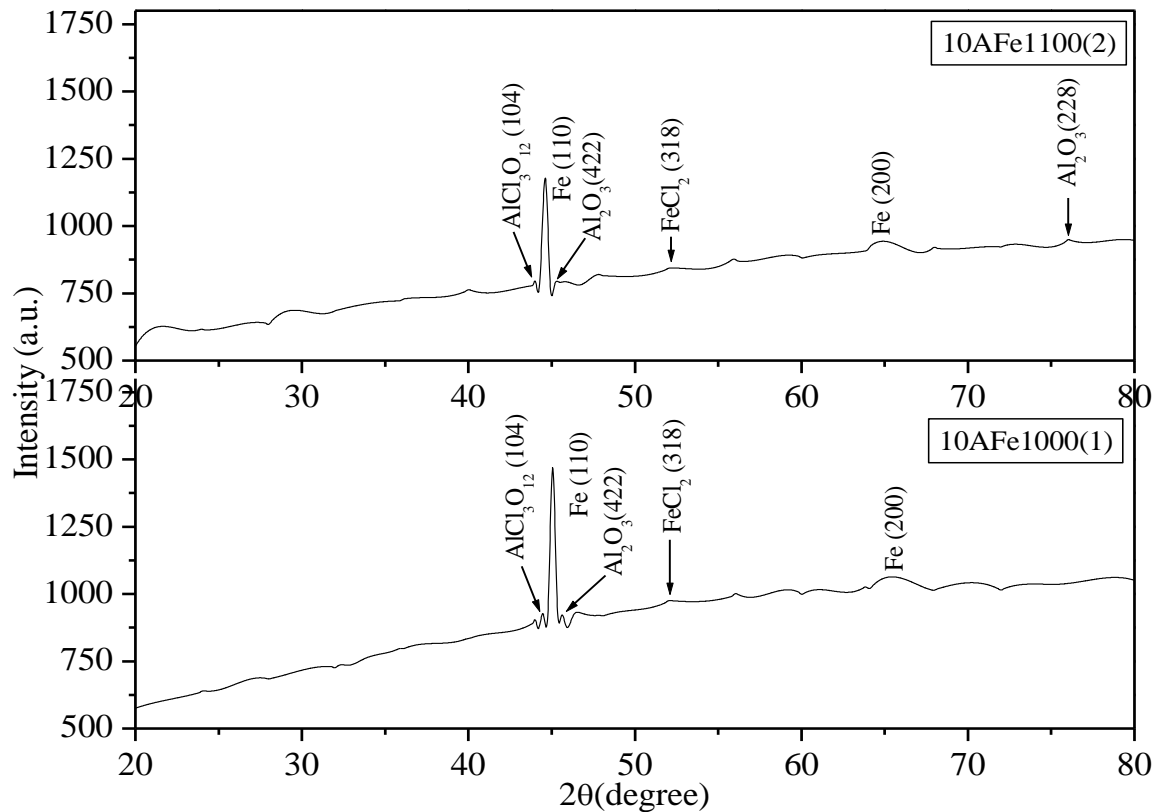


Figure 6: XRD plots of specimen 10AFe1000(1) and 10AFe1100(2) after corrosion in 1N HCl solution.

Scanning electron micrographs of the specimen were taken on the basis (i) Highest and lowest corrosion rate [Fig. 7 and 8] and (ii) Highest and lowest corrosion potential [Fig. 9 and 10]. Fig. 7 shows the SEM images of specimen 10AFe900(1) taken at (a) 500X (b) 2000X (c) 5000 X and (d) 15000 X magnifications after corrosion in 1N HCl solution. Microstructure at 500X shows the presence of intense patches formed due to the attack of HCl solution along with presence of some small size pores. The intensity of dark patches was so high that these could be very easily observed on the surface of the specimen. The micrograph of the same specimen at 2000X magnification is shown in Fig. 7(b) which shows the presence of the shattering of the conjugate particles along with the layering of the aluminium chlorate ($\text{AlCl}_3\text{O}_{12}$) particles. This aluminium chlorate particle forms by reaction between chlorine and alumina particles. Formation of the aluminium chlorate phase can be seen more clearly in the micrograph at 5000X [Fig. 7(c)]. It was observed that due to attack of HCl, elongation of the pores took place which can be seen very clearly in the micrograph shown in Fig. 7(d). The acid during the corrosion action has entered into the pores and it has led to their elongation. Since this specimen was sintered at lower temperature and for smaller time, the effect of acid attack was found to be more intense due to which the pore elongation and other distortions were generated on the specimen surface.

Fig. 8 shows the SEM of specimen 10AFe900(2) at (a) 500X (b) 2000X (c) 5000 X and (d) 15000X magnifications after corrosion in 1N HCl solution. The micrograph at 500X shows the distortion of the particles with presence of some light patches on the surface of the specimen. The less intensity of patches is due to less attack of the acid on the specimen in comparison to the specimen 10AFe900(1). Fig. 8(b) which is the micrograph of the same specimen at 2000X reveals the formation of the aluminium chlorate particles on the surface of the specimen and it also shows some minor distortion among the particles of the nanocomposite system. Grain refinement and lowering of the grain size has also been observed in this micrograph.

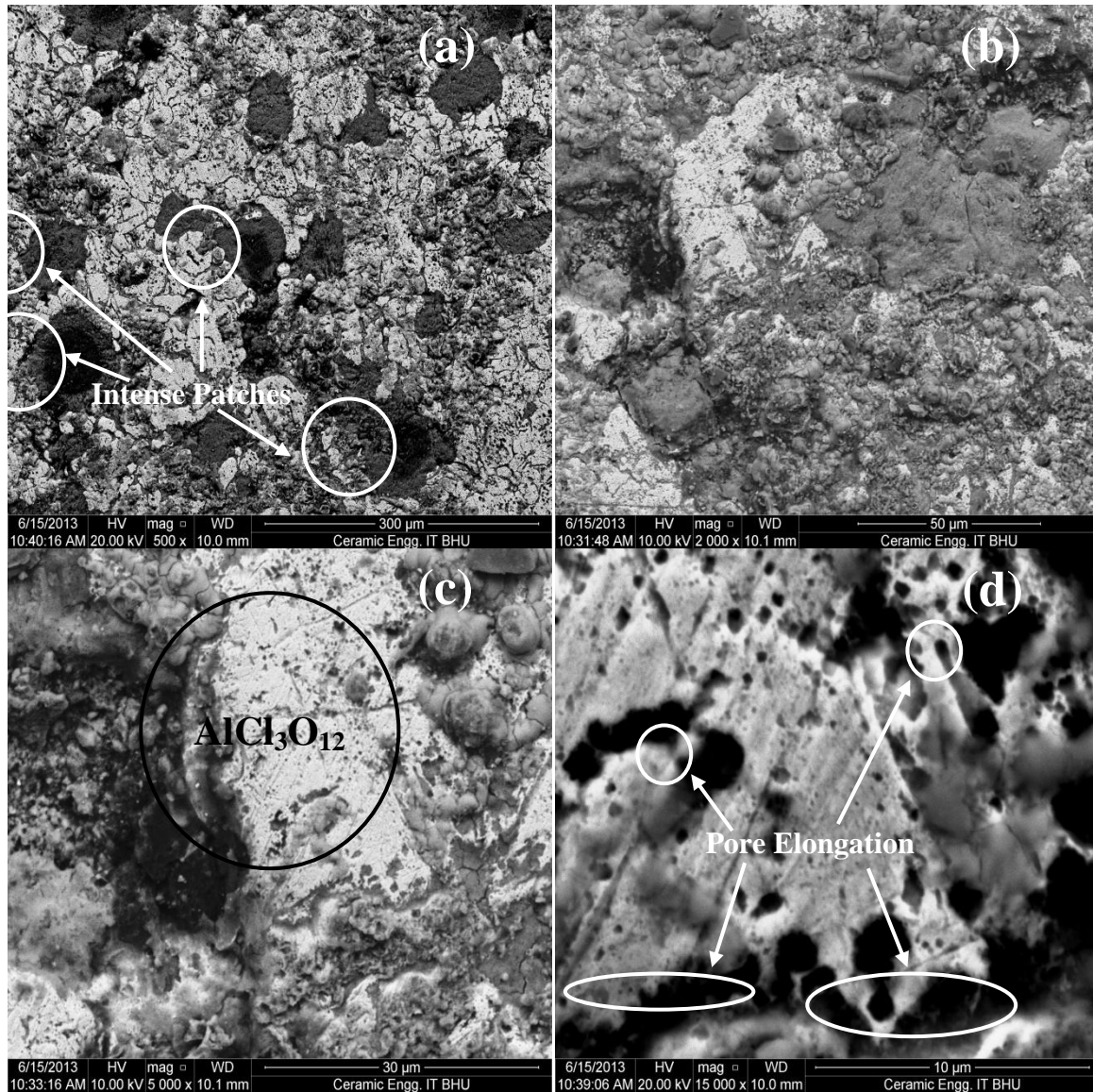


Figure 7: SEM of specimen 10AFe900(1) at (a) 500X (b) 2000X (c) 5000 X and (d) 15000 X magnifications after corrosion in 1N HCl.

Micrograph of the same specimen at 5000X is shown in Fig. 8(c) which shows some bigger particles of iron aluminate phase and some aluminium chlorate particles distributed in between the various particles. The micrograph at 15000X magnification is shown in Fig. 8(d) shows the strong bonding between the constituent particles which remain in intimate contact even due to the strong corrosion action. Therefore, it can be concluded that in the specimen 10AFe900(2), the complete reaction and an optimum amount of iron aluminate phase formation has taken place due to which the corrosion resistance is improved significantly. Due to improved corrosion resistance, formation of iron chloride phase cannot be distinguished clearly in the present micrograph.

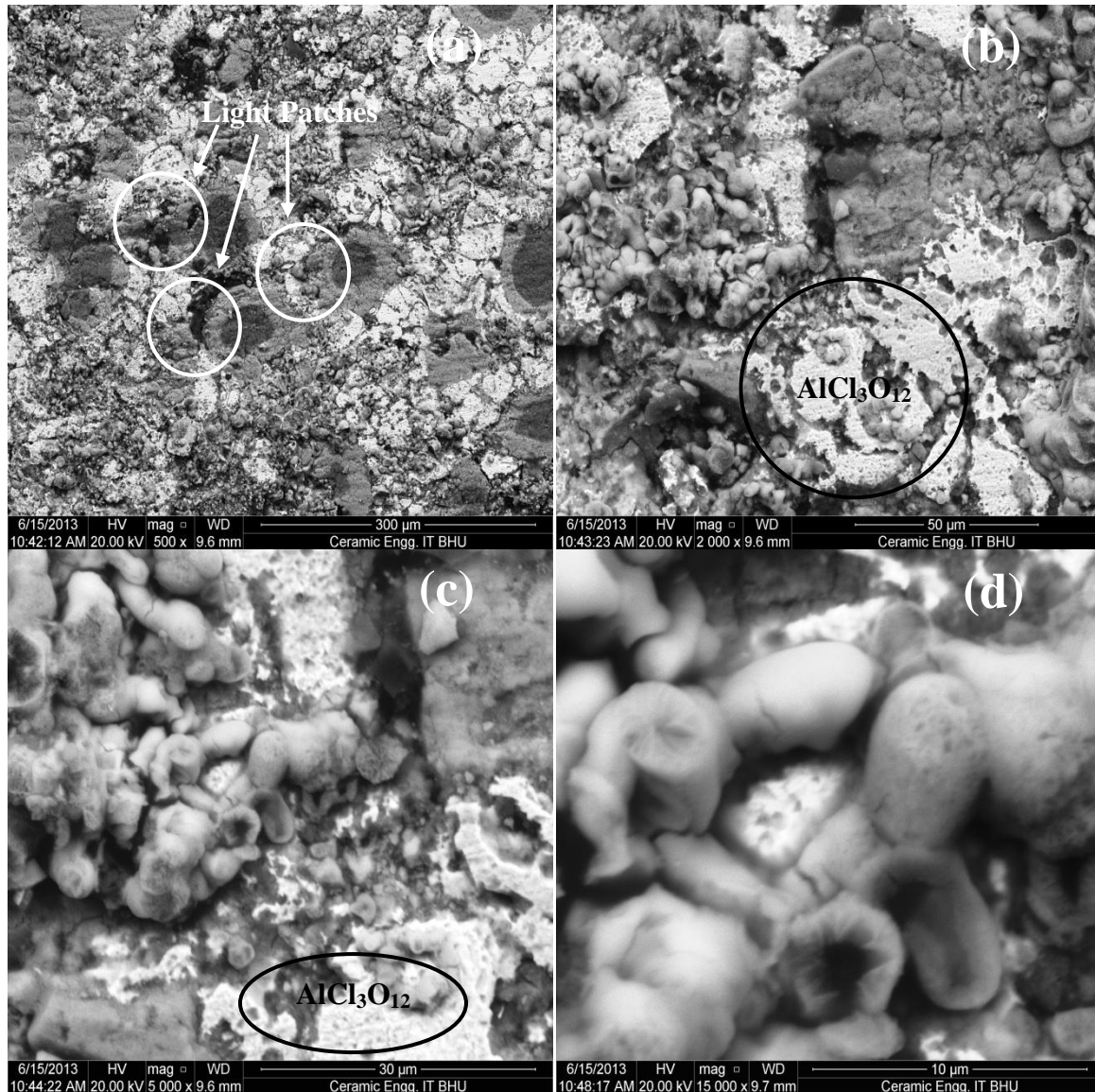


Figure 8: SEM of specimen 10AF900(2) at (a) 500X (b) 2000X (c) 5000 X and (d) 15000 X magnifications after corrosion in 1N HCl.

Fig. 9 illustrates the scanning electron micrographs of specimen 10AF1000(1) at (a) 500X (b) 2000X (c) 5000 X and (d) 15000X magnifications after corrosion in 1N HCl solution. This specimen shows the highest corrosion potential value. Micrograph of the specimen at 500X [Fig. 9(a)] shows the formation of some patches as well as the distributed type grains of the constituent particles. It also illustrates some micro cracks formed at the intergranular sites of the constituent particles. Fig. 9(b) shows the microstructure of the same specimen at 2000X magnification which shows an agglomeration amongst some particles of aluminium chlorate. It also shows that some particles are separated due to corrosion. This agglomeration can be due to very small size of the aluminium chlorate particles after completion of electrochemical activity on the nanocomposite specimen. Some non agglomerated particles are dispersed due to loosening of the bonds during the corrosion action. Formation of the aluminium chlorate phase can be seen much more clearly in Fig 9(c) which is the microstructure of the same specimen at 5000X magnification. It also shows reduction in grain size. The reduction in the grain size and formation of finer grains of iron aluminate phase can also be seen much more clearly in the micrograph at 15000X magnification [Fig. 9(d)].

Fig. 10 shows the SEM of specimen 10AFe1100(2) at (a) 500X (b) 2000X (c) 5000 X and (d) 15000 X magnifications after corrosion in 1N HCl solution. The present specimen shows the lowest corrosion potential.

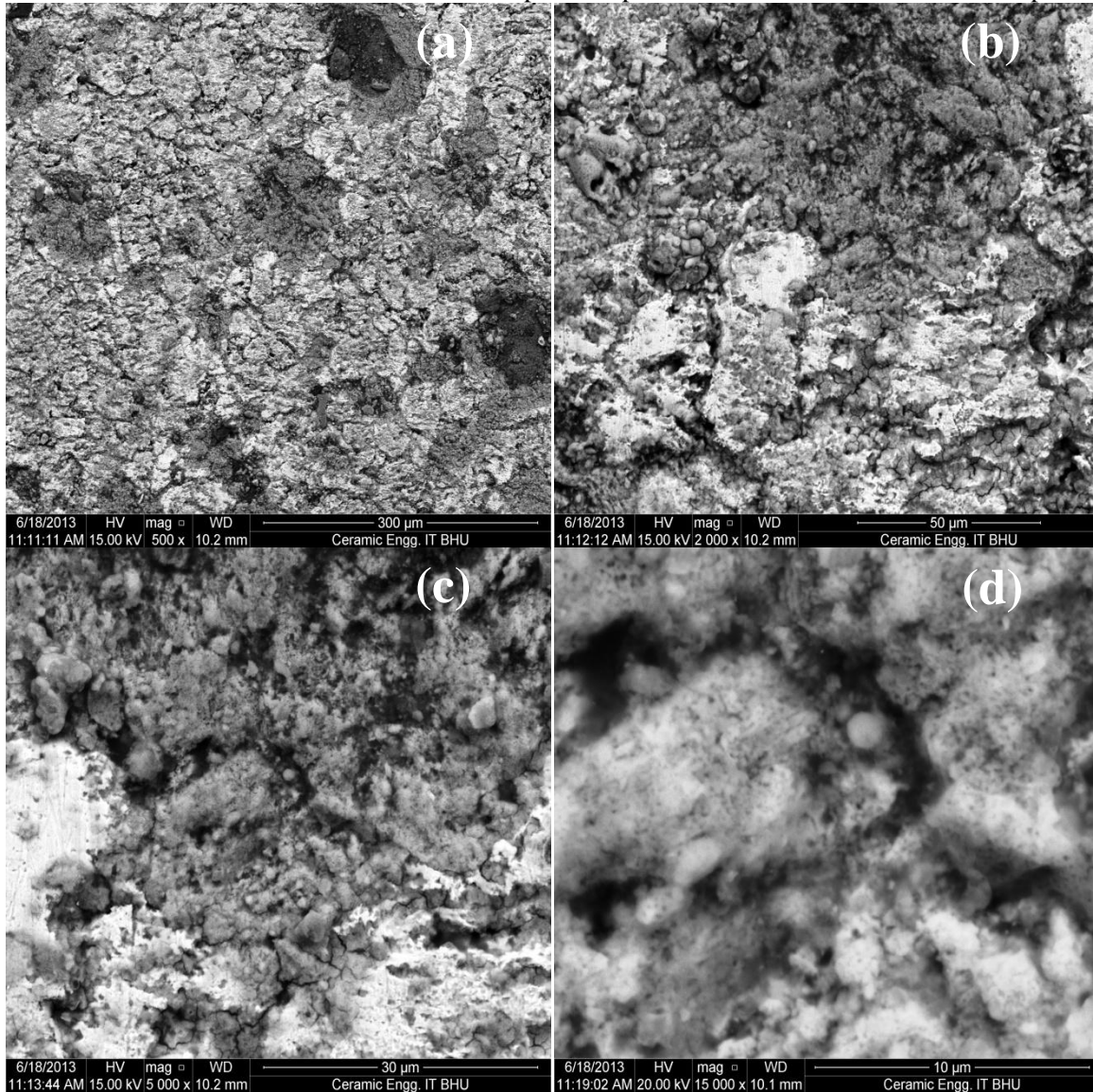


Figure 9: SEM of specimen 10AFe1000(1) at (a) 500X (b) 2000X (c) 5000 X and (d) 15000 X magnifications after corrosion in 1N HCl.

The scanning electron micrograph of the specimen at 500X magnification [Fig. 10(a)] shows the presence of the constituent particles along with some small cavities on the surface of the specimen. The outer periphery of the cavities is dark in nature. The cavities present on the specimen surface and the corresponding darkness present on the periphery are because of corrosion. The same micrograph when viewed at 2000X magnification as illustrated in Fig. 10(b) shows peeling of the material from the top surface of the specimen along with formation of some nano size aluminium chlorate phase deposited on the surface. Fig. 10(c) shows the SEM of the same specimen at 5000X magnification which shows the generation of a small number of particles of the constituent phase due to corrosion action. It also shows some wide patch of aluminium chlorate phase. The dispersed particles in the form of nano rods can be seen more clearly in the micrograph at 15000X magnification illustrated in Fig. 10(d). This micrograph also shows some iron chloride phase which is present in the dissolved form.

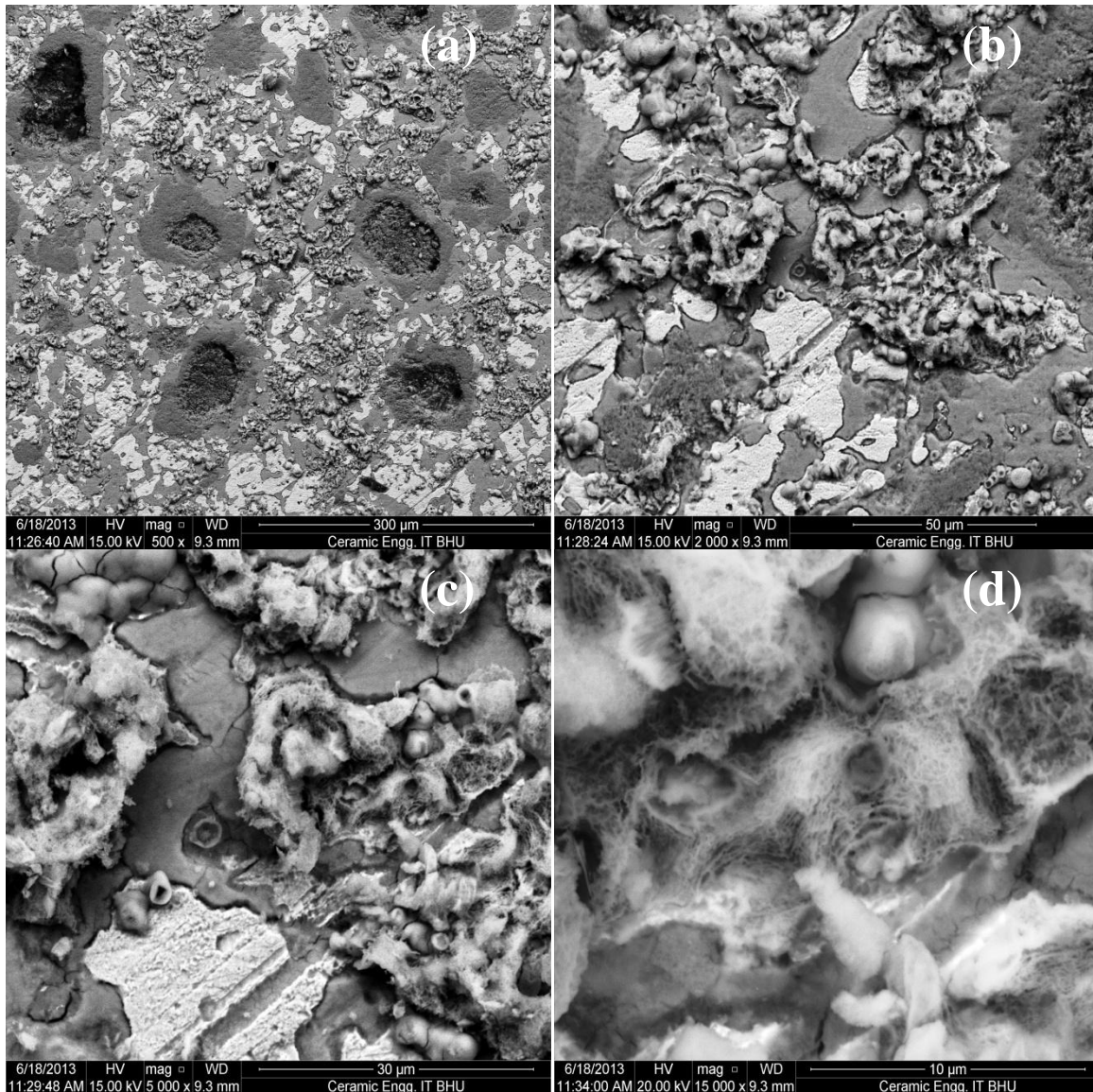


Figure 10: SEM of specimen 10AFe1100(2) at (a) 500X (b) 2000X (c) 5000 X and (d) 15000 X magnifications after corrosion in 1N HCl.

Conclusions

In the present paper an attempt has been made to study the effect of sintering parameters on the corrosion characteristics of iron-alumina metal matrix nanocomposites prepared by powder metallurgy technique. The experimental results have been discussed critically and the following important conclusions have been drawn:

- Iron aluminate (FeAl_2O_4) phase formation improved the corrosion resistance of Fe- Al_2O_3 metal matrix nanocomposite specimens.
- XRD results showed the presence of aluminum chlorate and iron chloride phases respectively in the corroded specimens.
- SEM results showed that the specimen having poor corrosion characteristics showed the formation of dark patches on the specimen surface.

Acknowledgements

Authors thankfully acknowledge the financial support received from Council of Scientific and Industrial Research, New Delhi. [I.I.T.(B.H.U.) Project No. GP/LT/Cer/13-14/01].

References

1. Harrigan Jr. W. C. *Mater. Sci. Engg. A.* 244(1998) 75.
2. Ralph B., Yuen H. C., Lee W. B. *J. Mater. Process. Tech.* 63 (1997) 339.
3. Rosso M. *J. Mater. Process. Tech.* 175 (2006) 364.
4. Tzamtzis S., Barekar N. S., Hari Babu N., Patel J., Dhindaw B. K., Fan Z. *Comp.: Part A* 40 (2009) 144.
5. Torralba J. M., Costa C. E., Velasco F. *J. Mater. Process. Tech.* 133 (2003) 203.
6. Moustafa, S.F., Abdel-Hamid, Z., Abd-Elhay, A.M. *Mater Let* 53 (2002) 244.
7. Rahimian M., Ehsani N., Parvin N., Baharvandi H. R. *J. Mater. Process. Tech.* 209 (2009) 5387.
8. Chen S. H., Wang T. C. *Acta. Mech.* 157 (2002) 113.
9. Yueguang, W. *Acta. Mech. Sinic.* 17 (2001) 45.
10. Miracle D. B. *Comp. Sci. Tech.* 65 (2005) 2526.
11. Kaczmar J. W., Pietrzak K., Wlosinski W. *J. Mater. Process. Tech.* 106 (2000) 58.
12. Candan S., Bilgic E. *Mater. Let.* 58 (2004) 2787.
13. Trzaskoma P. P., McCafferty E. *J. Elect. Chem. Soc.* 130(9) (1983) 1804.
14. Gupta P., Kumar D., Parkash O., Jha A. K. *Bull. Mater. Sci.* 36(5) (2012) 859.
15. Gupta P., Kumar D., Quraishi M. A., Parkash O. *Adv. Sci. Engg. Med.* 5(4) (2013) 366.
16. Jha P., Gupta P., Kumar D., Parkash O. *J Comp Mater* 2013; doi: 10.1177/0021998313494915.
17. Gupta P., Kumar D., Parkash O., Jha A. K. *J. Adv. Mater. Res.* 585 (2012) 584.
18. Gupta P., Kumar D., Quraishi M. A., Parkash O. *Adv. Sci. Engg. Med.* 5(12) (2013) 1279.
19. Gupta P., Kumar D., Parkash O., Jha A. K. *Proc. Int. Conf. Adv. Mater. Manuf. Tech.* ASME (2011) 1.

(2015); <http://www.jmaterenvironsci.com>